Highly infrared reflective nickel doped ZrO$_2$ from first principles simulation

Shizhong Yang[1,2], S.M Guo[3], Guang-Lin Zhao[1], and Ebrahim Khosravi[2]

[1]*Physics Department, Southern University and A & M College, Baton Rouge, Louisiana 70813*

[2]*Department of Computer Science, Southern University and A & M College, Baton Rouge, Louisiana 70813*

[3]*Department of Mechanic Engineering, Louisiana State University, Baton Rouge, Louisiana 70803*

Abstract

First principles（or *ab initio*） density-functional-theory (DFT) with projected augmented wave (PAW) method simulations were performed to calculate the electronic structures and optical properties of 25% nickel (Ni) doped cubic ZrO$_2$ crystals. We implemented two *ab initio* DFT application methods to the ZrO$_2$ ceramic elastic constant, structure stability, and optical property calculation. The Cerply-Alder type local density approximation（LDA）models show that the interstitial and substituting nickel doped ZrO$_2$ structures are metastable, through the elastic stability analysis, while the structure of 25% Ni doped at substitute site with a Zr vacancy is in a stable state. The reflectivity at different directions is evaluated by calculating the real and imaginary part of the dielectric constants. The result shows that the reflectivity of Ni doped ZrO$_2$ crystal, with a Zr vacancy structure, varies from 59% to 80% at (001) ~ (111) directions respectively. In comparison, the reflectivity of pure ZrO$_2$ is only 18% in the infrared wavelength range. The high reflectivity of 25% Ni doped ZrO$_2$ structure, with a Zr vacancy, is caused by the unique doped crystal structure and the associated vacancy charge state in this configuration.

I. INTRODUCTION

Zirconia (ZrO$_2$) stabilized by rare earth elements like Y^{3+} is often used as thermal barrier coatings (TBC)[1,2] in gas turbines, and rocket engines, due to its superior properties such as low thermal conductivity, chemically inert, and high corrosion resistance. Yttria-stabilized zirconia is also used as the solid electrolytes for solid oxide fuel cells. The stabilized ZrO$_2$ has a cubic fluorite structure at room temperature. Zirconia based TBCs are transparent or translucent to radiation wavelength in the 0.3µm~5µm range[3]. Because more than 90% of radiation is within this range at typical gas turbine temperatures of 1700~2000 ºK, to effectively reduce thermal radiation transport through TBC systems, thus to improve the thermal insulation function, researches have been carried out with emphasis to increase the photon scattering within the coating and to improve the coating's reflectivity property. Increasing the density of scattering defects, such as micro-cracks and pores within the coating, has been reported as an efficient way of reducing thermal radiation[4].

In solid oxide fuel cell (SOFC) application, Ni is usually used as an effective electron transport channel, while in TBC application Ni is added with Cr, Al, and Y as a buffer layer to form good binding and match the coefficient of thermal expansion between substrate and the ceramic top layer, mainly ZrO$_2$. An earlier theoretical simulation of carbon doped ZrO$_2$ containing interstitial or substitution carbon and zirconium vacancy was reported by Ivanovskii *et al.*[5]. *Ab initio* DFT method was successfully applied in ceramic elastic constant calculations[6,7,8], including cubic[6] and monoclinic ZrO$_2$[8]. However to the best of the authors' knowledge, no experimental and theoretical study has been conducted on the stabilized high concentration Ni

doped ZrO_2. In this report, we applied the stress-strain elastic constant calculation method, analyzed the three Ni doped ZrO_2 systems and concluded that the structure of 25% Ni doped at substitute site with a Zr vacancy is in a most stable structure. We also implemented an effective reflectivity (reflection coefficient) calculation method to the above Ni doped ZrO_2 system and our results show that at (111) of the doped ZrO_2, the reflectivity in infrared range reaches 80%.

II. COMPUTATIONAL METHODS

In this report, *ab initio* DFT with the projector augmented wave (PAW) plane-wave method [9, 10], relativistic effect was considered, was used to calculate the elastic constant and electronic properties of ZrO_2 composites. The local density approximation (LDA) and Ceperley-Alder potential (quantum Monte Carlo based) [11] was used in this study. For O atoms, the 2s and 2p electrons were described as valence, for Zr the 4s, 4p, 4d, and 5s electrons were treated as valence, whereas for Ni the 3d and 4s electrons were treated as valence. The remaining electrons were kept in a frozen core. The calculated total energies converged to a value less than 1meV while using the plane wave energy cutoff of 450 eV. With this setting and a 12 x 12 x 12 *k*-space Monkhost grid, the lattice constant of ZrO_2 crystal is found to be *a* = 5.062 Å, in excellent agreement with the value 5.07 Å published in JCPDS file 7-337 for cubic zirconia. All of our calculations are based on the same potential, energy cutoff, energy and residue force convergence criteria as those used in the lattice constant calculations.

(a)

(b)

Figure 1. (a). The Ni doped at a substitution site with a Zr vacancy; and (b) pure ZrO_2 unit cell. The blue sphere stands for Ni atoms, the light green sphere represents the Zr atoms, and the red sphere stands for oxygen atoms.

The unit cell models are shown in Fig. 1. In all of the electronic calculations presented in this report, the *k*-space sampling uses 12 x 12 x 12 Monkhost grid. The electronic energy convergence value was set to be 10^{-5} eV and the residue force was set to be 1meV/Å. The unit cell shape, size, and atomic coordinates of the systems were relaxed in the optimization process. To save computer time, symmetry was considered in all of the elastic constant calculations.

There are two *ab initio* methods to calculate the elastic constants. One is the fitting method by fitting the total energies with respect to related strains near the ground state energy. The other is a straight forward method by analyze the stress-strain relations. This method can be traced back to the work of Nielson and Martin[12]. According to Hooks law, the stress component σ_i (i=1~6) is in linear dependency of the applied strain ε_j (j=1~6) under a small deformation:

$$\sigma_i = C_{ij}\, \varepsilon_j \tag{1}$$

The linear elastic constants C_{ij} form a 6 × 6 symmetric matrix, having 27 different components. Due to symmetry, a cubic crystal has only three different symmetry elements (C_{11},

C_{12} and C_{44}), each of which represents three equal elastic constants ($C_{11}=C_{22}=C_{33}$; $C_{12}=C_{23}=C_{31}$; $C_{44}=C_{55}=C_{66}$)[13]. Properties such as the bulk modulus and shear modulus can be computed from the values of C_{ij}. Methods to determine the elastic constants from first principles usually involve setting the strain to a finite value, re-optimizing any free parameters and calculating the stress. By carefully choosing the applied deformation, elastic constants can then be determined. The deformation value needs to be tested before final calculation is done. Too big deformation may cause nonlinear effect, while too small deformation could also induce large force error. In our Ni doped ZrO_2 calculation, we limit our deformation maximum to be 0.01. The stress-strain elastic constant calculation method allows us to predict elastic constants for new materials, materials where experimental data do not exist, and to resolve discrepancies between contradictory experimental results.

Under the same setting, after the structure optimization, the optical dielectric tensor was calculated by Fermi golden rule using PAW method. The imaginary part (ε_2) was calculated first, then the real part was deduced by Kramers-Kronig transform. The reflectivity R was calculated by

$$R = \left[\frac{1-N}{1+N} \right]^2 ,$$ (2)

where N is the reflective index which can be evaluated by:

$$N^2 = \varepsilon_1 + i\varepsilon_2 ,$$ (3)

in which ε_1 and ε_2 are the real and imaginary parts of the complex dielectric constant. The spin polarization was considered in all of the calculations.

IIIa. RESULTS OF CALCULATED ELECTRONIC STRUCTURE

To validate the simulation software, the lattice constant and bulk modulus of pure ZrO_2 was calculated first. Excellent agreement was found between the predicted ZrO_2 lattice constant and the corresponding experimental results. Based on the settings used in the validation lattice calculation, further calculations were performed on the elastic constants for pure ZrO_2, Ni interstitial and substitution site doped ZrO_2, and Ni substitution site doped with a Zr vacancy ZrO_2 crystal. To have a stable cubic structure, the following conditions[13] should be held for each test case,

$C_{44}>0$, $C_{11}>|C_{12}|$, and $C_{11}+2C_{12}>0$ (4)

The calculation results show that the C_{44} of both Ni interstitial and substitution site doped structures are negative, i.e. they are meta-stable structures. Thus only pure and Ni substitution site doped with a Zr vacancy ZrO_2 crystals (the term "Ni doped ZrO_2" is used for this case hereafter) were reported in Table I for elastic constant values.

The optimized lattice constants of Ni doped ZrO_2 are a=b=5.27 Å, c=4.20 Å, that are 4% larger and 17% smaller than that of the pure ZrO_2 crystal value of 5.07 Å. The calculated total magnetic moment is very small (less than 0.005 μ_B). It can be seen from Table I that the Voigt bulk modulus of experiment is 212.33 GPa, which is close to our result of 226.89 GPa in the simulation. The C_{11}, C_{33}, and C_{44} of Ni doped ZrO_2 decrease tremendously compared to their pure ZrO_2 values, i.e. from 532.15, 532.15, and 55.70 GPa to 139.31, 128.26, and 0.23 GPa respectively. While the C_{66} value only has a minor decrease, from 55.70 GPa to 38.03 GPa,

comparing to the above mentioned large variations. The calculated Bader charge[14] results of both systems are listed in Table II.

Table I. Elastic constants of pure and Ni doped ZrO_2 (in GPa). B_v stands for Voigt bulk modulus, while S_v stands for Voigt shear modulus. Temperature unit is in K, Y_2O_3 is in mol% ratio.

System	Temperature	Y_2O_3	C_{11}	C_{12}	C_{13}	C_{33}	C_{44}	C_{66}	B_v	S_v	Ref
Experiment	300	8%	413	112	112	413	61	61	212.33	96.80	(Ref. [15])
	300	8%	394	91	91	394	56	56	190		(Ref. [16])
	300	18%	375	75	75	375	64	64			(Ref. [17])
	300	15%	475	144	144	475	61	61			(Ref. [18])
	300	8.1%	402	95	95	402	56	56			(Ref. [19])
Theory	0	0%	500±100	90±20	90±20	500±100					(Ref. [6])
	0	0%	222	61	61	222	54	54	115		(Ref. [20])
	0	0%	455	64	64	455	63	63			(Ref. [21])
Pure ZrO_2	0	0%	532.15	74.24	74.24	532.15	55.70	55.70	226.89	125.00	this work
Ni doped ZrO_2	0	0%	139.31	133.27	75.36	128.26	0.23	38.03	108.32	15.89	this work

Table II. Bader charge of pure and Ni doped ZrO_2. (in unit of electron charge $|e|$)

System	Zr	O	Ni
Pure ZrO_2	2.64	-1.32	N/A
Ni doped ZrO_2	2.58	-0.81~-0.85	1.45

Figure 2 shows the electron density of states (DOS) of s and p orbitals of Zr and O for pure and Ni doped ZrO_2. The Fermi level is set at 0.0eV. The p_z component of Zr in Fig. 2(a) and 2(b) has shown a down-shift near -2eV. The p_y intensity near 2eV increases slightly. Comparing the p_z DOS of O atoms in Fig. 2(c) and 2(d), it is clear that in pure ZrO_2, p_z extends from -6eV to -0.5 eV below Fermi level with two major peaks at -5.3 eV and -1.2eV, while in Zr doped ZrO_2, p_z state of O atom extends from about -7.2 eV up to 2eV above the Fermi level with a small peak at 1.3 eV. Similarly p_y and p_x also show band extension from below Fermi level to 1eV above and from -7 eV to -6 eV. In Fig. 3(a) and 3(b), the Zr d_{xy}, d_{yz}, and d_{xz} are mainly located below the Fermi level in both pure and Ni doped ZrO_2 with extension to +2eV and -7 eV. The Zr d_{z^2} and d_{x^2} of Ni doped ZrO_2 are also more extended, comparing to the pure ZrO_2 case with the peaks sitting at 3.5eV and 4 eV. Thus it is clear that the p orbitals of O are hybridized with p and d_{xy}, d_{yz}, and d_{xz} orbitals of Zr with energy range extended to higher and lower energy scales.

Fig. 3(c) shows that the symmetric nature of the spin up and down states of Ni d orbitals makes the total magnetic moment zero. The d_{z^2} and d_{x^2} orbitals of Ni atom are below Fermi level which is different from that of Zr d_{z^2} and d_{x^2} where both are above the Fermi level, while the d_{xy}, d_{yz}, and d_{xz} orbitals are extended to both higher and lower energy scales similar to that in Zr.
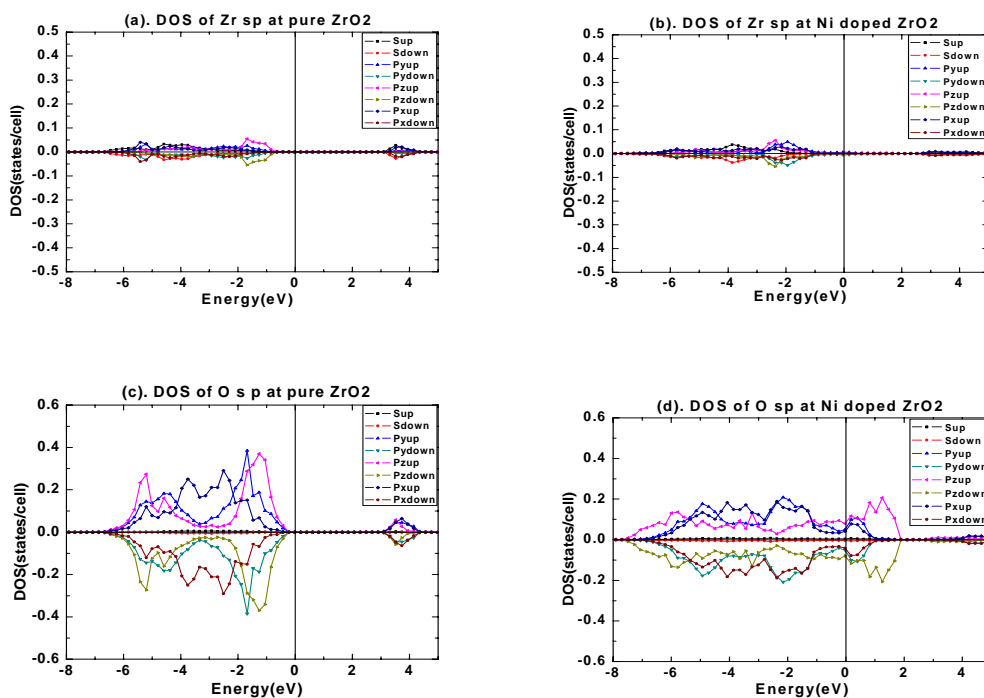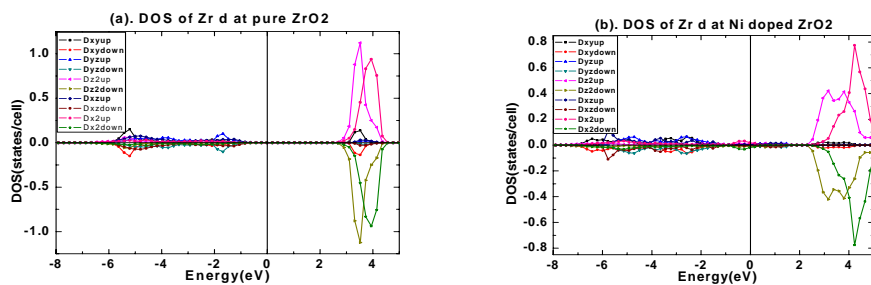
Figure 2. The partial DOS of s and p states of Ni doped and pure ZrO_2. The black square stands for s states with spin up, the red circle stands for s states with spin down; blue upward triangle for p_y electron with spin up, light green downward triangle for p_y down, pink leftward triangle for p_z up, gold rightward triangle for p_z down, cyan diamond for p_x up, while the brown pentagon for the p_x with a down spin.
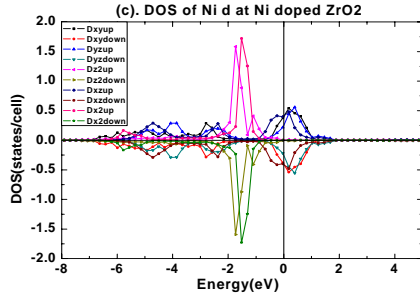
Figure 3. The partial DOS of d states in Ni doped and pure ZrO_2. The black square stands for d_{xy} states with spin up, the red circle stands for d_{xy} states with spin down; blue upward triangle for d_{yz} with spin up, light green downward triangle for d_{yz} down, pink leftward triangle for d_{z^2} up, gold rightward triangle for d_{z^2} down, cyan diamond for d_{xz} up, brown pentagon for d_{xz} down, light red hexagon for d_{x^2} up, while green star for d_{x^2} down.

III b. OPTICAL PROPERTY RESULTS

The electromagnetic reflectivity properties of pure and Ni doped ZrO_2 are shown in Fig. 4(a) and 4(b). The reflectivity data of pure ZrO_2 at (010) direction was ignored in Fig. 4(a) since it has the same curve as in (001) direction. From Fig. 4 (a) and (b), it can be seen that the reflectivity is increased from (001), (011), to (111) direction for both pure and Ni doped ZrO_2 crystals. It can also be seen from Fig. 4(a) and 4(b) that the reflectivity of Ni doped ZrO_2 increased by 3.4, 4.1, 2.6, and 2.3 times in comparison to pure ZrO_2 cases along the (001), (010), (011), and (111) polarization directions respectively.
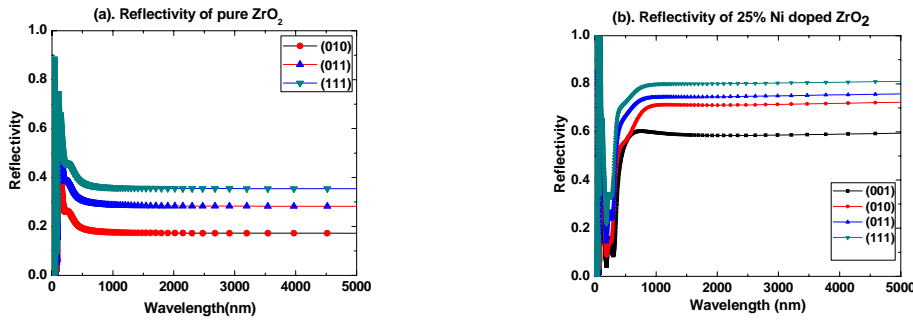

Figure 4. (a). The reflectivity of pure ZrO_2. (b). The reflectivity of 25% Ni doped ZrO_2. The black squares stand for the reflectivity in (001) direction. The red circles stand for the reflectivity in (010) direction. The up blue triangles stand for the reflectivity in (011) direction. The down triangles (in dark cyan color) stand for the reflectivity in (111) direction.

IV. DISCUSSION AND CONCLUSIONS

From Table I, we can see that most experimental elastic constant data of cubic ZrO_2 were measured at near 8% Y doped and room or higher temperatures while our calculation for the cubic ZrO_2 contains 0% Y at zero temperature, we would expect some differences between experimental data and our calculation results. Actually our calculated C_{12}, C_{44} results are close to the data at Reference 16. The C_{11} is off the experimental data but is in the range of former *ab*

initio DFT calculation presented in Reference 6. From Table I we can also see that among the methods of *ab initio* DFT, muffin-tin(MT) approximation with free electron gas pair potential, and lattice dynamics, the *ab initio* DFT method is the best one which gives good agreement with the corresponding experimental data. This is due to the two body pair potential approximation used in the MT method and the empirical data included in the lattice dynamics method, while in *ab initio* DFT method, no empirical data was used.

From Fig. 3(c) and Fig. 2(d), it is clear that near the Fermi level, the Ni d_{z^2} and d_{x^2} orbitals hybridize with O p_y, and p_x orbitals, and thus form chemical σ bonding, as can be seen that these Ni d and O p bands reach their DOS peaks in the energy region of -2.0 ev ~ -1.5 eV. The Ni d_{xy}, d_{yz}, and d_{xz} orbitals, on the other hand, hybridized with O p_y, p_z, and p_x orbitals at π bonded states in the energy range of both below and above Fermi level. As shown in Fig. 2 and 3, the p orbitals of O are hybridized with Zr p orbitals and d_{xy}, d_{yz}, and d_{xz} orbitals. An important effect of the Ni doping is that, as can be seen from Fig. 2(d) and 3(c), both O and Ni atom form states above and close to the Fermi level. These states can effectively serve as recombination and scattering centers when electromagnetic waves enter the system. The total magnetic moment of Ni atom is zero due to the symmetric spin up and down DOS of Ni d orbital as discussed in the last section.

Table II listed the Bader charge of Zr, O, and Ni in pure and Ni doped ZrO_2. The Bader charge of Zr cation decreases slightly from 2.64|e| in pure ZrO_2 to 2.58|e| (loses less than 0.1|e| charge) in Ni doped ZrO_2 whereas O anion increased from -1.32|e| to -0.81~-0.85|e| with an average of 0.5|e| charge gain. The substitution Ni cation has a 1.45|e| which is about one electron charge less than Zr cation. O anion charges changed due to the less charge of Ni and the Zr vacancy formation. The larger charge difference of O is consistent with the large shift and extension of DOS shown in Fig. 2(c) and 2(d).

The high Ni doping concentration and Zr vacancy cause the formation of large scale localized dipoles around vacancies. The local electric field is stronger at (111) direction than that of (011) and (001) directions as from the above Ni, Zr and O Bader charge analysis. In each unit cell there are two opposite dipoles pointing from the center of $O^{-0.8}$ to the center of $Ni^{+1.45}$ (vacancy). The electromagnetic waves thus are interacted strongly with these high density localized dipoles.

In summary, we implemented two *ab initio* DFT application methods to the ZrO_2 ceramic calculation: (1) elastic constant calculation and application to the structure stability analysis; (2) the reflectivity along special directions of the related systems. They can be essential to the systems where experimental data is not available or cannot be acquired under current conditions. In the DFT based simulations on a Ni doped ZrO_2 system, the lattice constant of pure ZrO_2 is examined first, which compares very well with the experiment data. Then the elastic constants for a number of cases are calculated, which include the pure ZrO_2, 25% Ni interstitial and substitution site doped cubic ZrO_2 crystals, and 25% Ni substitute site doped cubic ZrO_2 crystal with a Zr vacancy. The elastic constant results demonstrate that only pure ZrO_2 and 25% Ni substitution site doped cubic ZrO_2 crystal with a Zr vacancy are stable structures. Thus the reflectivity calculations are performed on these two systems only. The reflectivity calculations clearly show that the high concentration Ni doped ZrO_2 increased the reflectivity values by 3.4, 4.1, 2.6, and 2.3 times in (001), (010), (011), and (111) polarization directions respectively, with a maximal 80% reflectivity at (111) direction. This may have potential applications in high efficient TBC material design and synthesizing.

References:

[1]. D. A. Litton, N. E. Ulion, M. F. Trubelja, M. J. Maloney, and S. G. Warrier, United States Patent No. 6,730,422 (2004).

[2]. R. Gadow and G. Schaefer, United States Patent No. 6,998,064 (2006).

[3]. J. I. Eldridge, C. M. Spuckler, and K. W. Street, Infrared Radiative Properties of Yttria-Stabilized Zirconia Thermal Barrier Coatings, 26th Annual Conference of Composites, Advanced Ceramics, Materials and Structures: B, (Cocoa Beach, Florida, 2002, American Ceramic Society, Westerville, OH), p 417.

[4]. S. Gu, T. J. Lu, D. D. Hass, H. N. G. Wadley, Acta Mater. **49**, 2539 (2001).

[5]. A. L. Ivanovskii, S. V. Okatov, and G. P. Shveikin, Inorganic Materials **36**, 1121 (2000).

[6]. H. J. F. Jansen, Phys. Rev. B **43**, 7267 (1991).

[7]. H. Yao, L. Ouyang, and W. Y. Ching, J. Am. Ceram. Soc. **90**, 3194 (2007).

[8]. M. Iuga, G. S. Neumann, and J. Meinhardt, Eur. Phys. J. B **58**, 127 (2007).

[9]. P.E. Blöchl, Phys. Rev. B **50**, 17953 (1994).

[10]. G. Kresse and D. Joubert, Phys. Rev. B **59**, 1758 (1999).

[11]. D. M. Ceperley and B. J. Alder, Phys. Rev. Lett. **45**, 566 (1980).

[12]. H. Nielsen and R. M. Martin, Phys. Rev. Lett. **50**, 697 (1983).

[13]. F. Nye, Physical properties of crystals, Oxford, Clarendon, 1957.

[14]. R. F. W. Bader, in Atoms in Molecules -- A Quantum Theory, Oxford University Press, Oxford, 1990.

[15]. D. E. Ellis, K. Mundim, V. P. Dravid, and J. W. Rylander, pp350-64 in Computer Aided Design of High-Temperature Materials, Oxford University Press, Oxford, U.K. 1999.

[16]. T. Hailing and G. A. Saunders, J. Mater. Sci. Lett. **1**, 416 (1982).

[17]. S. Shin and M. Ishigame, Phys. Rev. B **34**, 8875 (1986).

[18]. D. W. Liu, C. H. Perry, A. A. Feinberg, and R. Currat, Phys. Rev. B **36**, 9212 (1987).

[19]. H. M. Kandil, J. D. Greiner, and J. F. Smith, J. Am. Ceram. Soc. **67**, 341 (1984).

[20]. L. L. Boyer and B. M. Klein, J. Am. Ceram. Soc. **68**, 278 (1985).

[21]. A. P. Mirgorodsky, M. B. Smirnov, and P. E. Quintard, Phys. Rev. B **55**, 19 (1997).